

Dielectric spectroscopy on 2D and 3D metal halide perovskites
using an interdigitated electrode geometry

Carrie Emma McClure

A senior thesis submitted to the faculty of
Brigham Young University
in partial fulfillment of the requirements for the degree of
Bachelor of Science

John Colton, Advisor

Department of Physics and Astronomy
Brigham Young University

Copyright © [2022] Carrie Emma McClure

All Rights Reserved

ABSTRACT

Dielectric spectroscopy on 2D and 3D metal halide perovskites
using an interdigitated electrode geometry

Carrie Emma McClure
Department of Physics and Astronomy, BYU
Bachelor of Science

Metal halide perovskites are a class of 2D and 3D materials that are currently being studied for use in solar energy and other applications. Permittivity is connected to other important characteristics of these materials such as exciton binding energy, effective mass, and transition dipole moment, but has proven challenging to accurately measure. Using experimental measurements of the impedance of perovskite layers on interdigitated electrodes, we have been able to develop a model which allows us to deduce the frequency dependence of permittivity in these materials. The results show permittivity values for high frequencies (13 MHz) in the range of 4.1-5.1 for PEA_2PbI_4 (PEPI) and 12-45 for MAPbI_3 (MAPI), with details depending on the specific sample. Further work will allow some of the first measurements of dielectric constant in this frequency range for several types of perovskites, aiding computational modeling and experimental electroabsorption analysis.

Keywords: perovskite, halide, permittivity, dielectric constant, spectroscopy, interdigitated electrode, electroabsorption, exciton binding energy, impedance, capacitance, low frequency

ACKNOWLEDGMENTS

I would like to thank all of those who have made my research possible, including my parents Amy and David McClure, as well as my faculty advisor Dr. John Colton. A special thanks for Kameron Hansen, who taught me nearly everything I know about perovskites and helped me kick this project off from his research. And thanks to all of the other research students in the group who have worked with me over the years.

Contents

Table of Contents	vii
1 Introduction	1
1.1 Metal halide perovskites in solar technology	1
1.2 Physical, electronic, and optical properties of perovskite materials	4
1.3 Benefits and requirements of the electroabsorption technique	6
1.4 The absence of permittivity data on perovskites	7
1.5 Relationship between permittivity and capacitance	10
1.6 Parallel plate electrode geometries	11
1.7 Adjacent electrode geometries	14
2 Development of Mathematical Model	17
2.1 Interdigitated electrode geometries	17
2.2 New approach to 3D interdigitated electrode model	19
2.3 The mathematical model for capacitance	20
3 Testing Model on Quartz and Water	29
3.1 Measurements on quartz substrate	29
3.2 Measurements on water	32
4 Dielectric Constant Measurements on Perovskites	37
4.1 Sample preparation on electrodes	37
4.2 Measurements on MAPI	39
4.3 Measurements on PEPI	41
4.4 Measurements on PEPBr and PEPCl	43
5 Conclusion	45
5.1 Discussion	45
5.2 Future work	46
Bibliography	47

Chapter 1

Introduction

1.1 Metal halide perovskites in solar technology

Metal halide perovskites are a class of material comprising layers of octahedral inorganic crystalline lattices of metal plus halogen atoms, interrupted by layers of organic molecules. The specific atoms and molecules involved in perovskites can be varied, as well as the layering pattern: perfectly alternating perovskites with $n = 1$ crystalline layers per organic layer create a “2D” material that can be considered quantum wells, while large assemblies of $n > 1$ and $n = \infty$ crystalline layers per organic layer create a more “3D” material, as depicted in Fig. 1.1. All of these variable factors mean that perovskites don’t have just one specific set of electrical or optical properties, but rather a continuum that can be tuned for desired effects [1].

The perovskites that will be addressed in this thesis are lead based, although we are also beginning to study their tin-based counterparts. While tin-based perovskites have an optical bandgap that is ideal for many solar cells, they are also much trickier to study since the small distances between their optical features are easily obfuscated by thermal broadening effects [2]. The two predominant perovskites in this thesis are methyl-ammonium lead iodide (MAPbI₃, MAPI), a

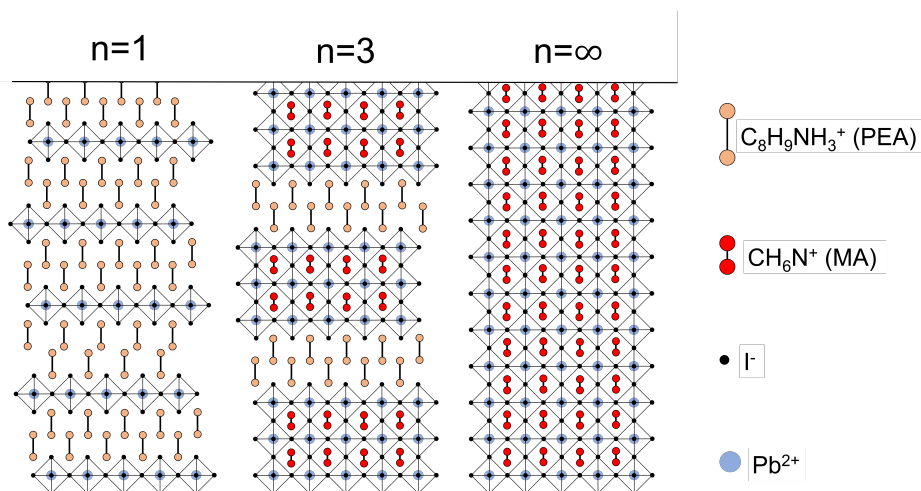


Figure 1.1 Series of crystalline structures of the perovskites PEPI $n = 1$, PEPI $n = 3$, and PEPI $n = \infty$ (i.e. MAPI). Each of these materials are made from a different number of octahedral inorganic layers separated by organic cation layers. When $n = 1$, the material is "2D", and as the number of successive inorganic octahedral layers increases, the material becomes a "3D" material.

3D perovskite, and phenethyl-ammonium lead iodide (PEA_2PbI_4 , PEPI), a 2D perovskite, although two halide variants will also be discussed briefly.

Perovskite materials have already shown great promise for use in solar technology despite only growing in popularity in the scientific community in the last decade or so. The quantum efficiency of perovskites, a value that quantifies their ability to capture solar energy, has grown from 14.1% to 25.7% in just seven years; for comparison, it has taken crystalline silicon solar cells 25 years to increase by just 2% [3]. As of 2018, the efficiency of crystalline silicon sits around 26.1%, well within range of the predicted trajectory of perovskites within the next several years [3]. The quantum efficiencies of these materials are also relatively large in comparison to many other solar cell materials, including other crystalline and amorphous structures as well as quantum dots, as depicted in Fig. 1.2.

Although perovskite materials show great potential for use in solar and other technology, there are many factors delaying their use, including gaps in the knowledge required to fully understand

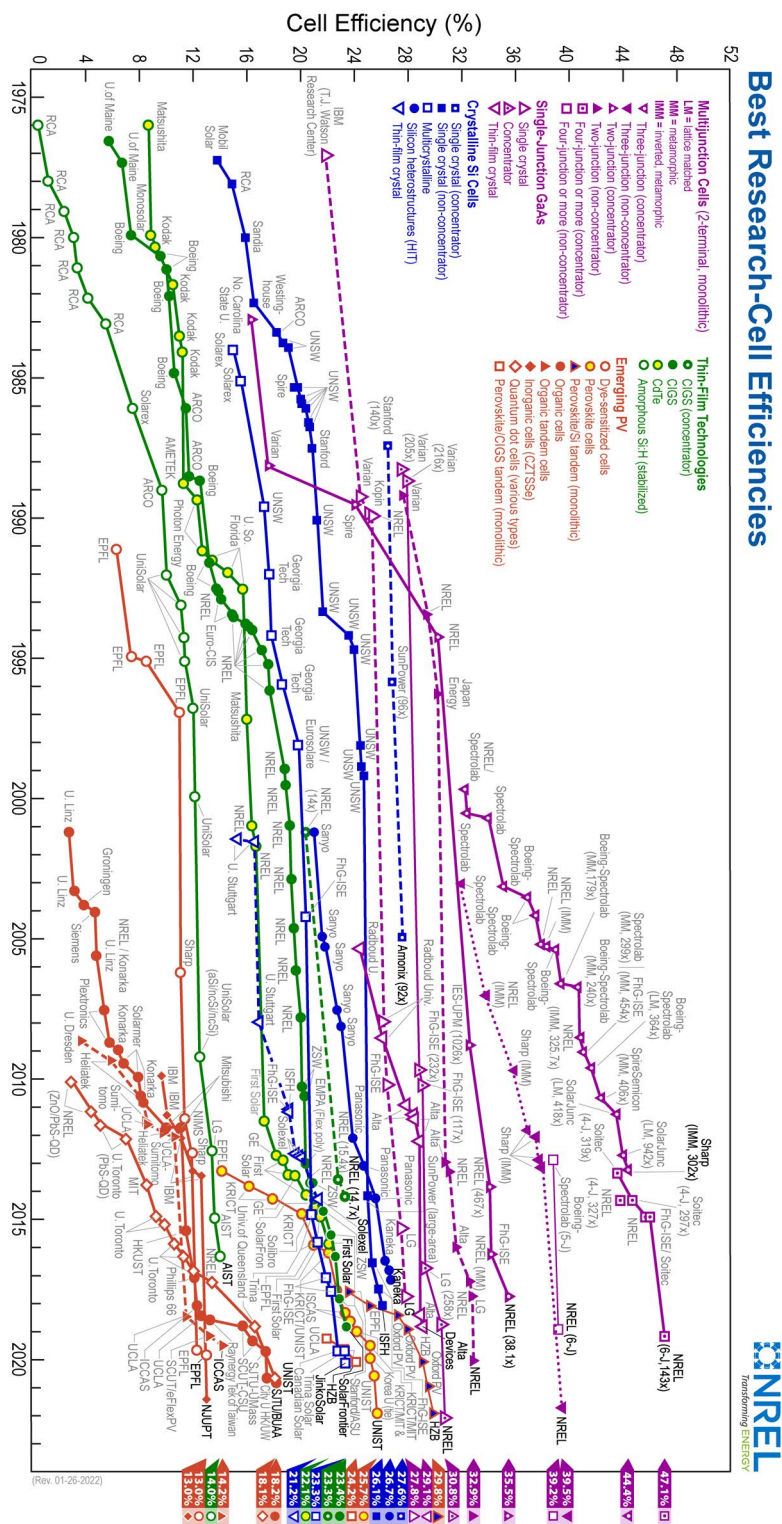


Figure 1.2 Solar cell efficiencies plotted vs. year for many classes of materials. Perovskite solar cells have shown a sharp increase in quantum efficiency in just one decade, approaching that of the traditional silicon solar cell. Figure from [3].

these materials and issues in practicality that have yet to be overcome. Optical quantities such as band gap and exciton binding energy have been reported on many types of perovskites, but do not reach a clear consensus due to experimental challenges in their measurement. Other quantities, such as permittivity, have only been measured on select perovskites, in select frequency ranges. The work of studying these materials is ongoing in the scientific community, utilizing a variety of measurement and analysis techniques.

1.2 Physical, electronic, and optical properties of perovskite materials

Perovskites are direct bandgap semiconductors, where the transition of an electron from the conduction band to the valence band produces a photon equal in energy to the energy difference in states. Electrons in the conduction band will settle to the lowest energy state possible within a very short amount of time, and holes in the valence band will rise to the highest energy state available, so the typical energy difference between bands is a near-constant value called the bandgap. When materials with a direct bandgap are excited with a laser, they emit photoluminescence at this single wavelength, creating a sharp peak in the data. In absorption data, the bandgap instead is indicated by an energy step-function where photons of greater energy will be accepted into the system to excite an electron, but photons of smaller energy cannot. These relationships are shown in Figure 1.3 for two common perovskites. Optical data on perovskites show these features resulting from the bandgap, but additionally exhibit features caused by a quasiparticle called the exciton that is also important to study due to its influence in the process of solar energy conversion.

The exciton is a quasiparticle described by a bound state between an electron and an electron hole in a material. There are different types of excitons that are classified by their behavior and characteristics, but measurement of their energies are some of the most important pieces of

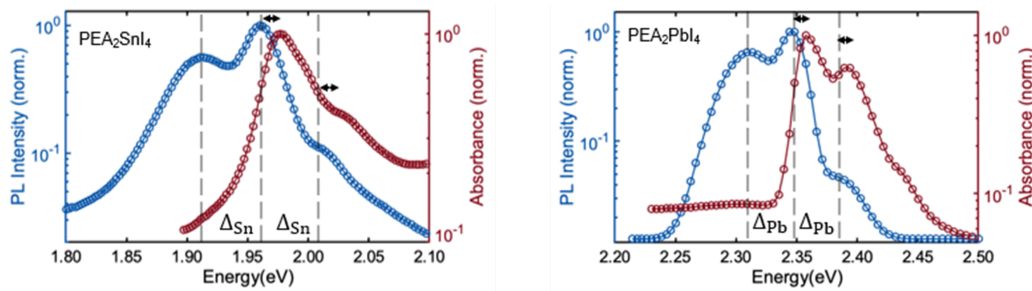


Figure 1.3 Plots demonstrating the relationship between photoluminescence spectra (blue) and absorption spectra (red) on PESA and PEPI perovskites. Absorption measurements probe the energies of light accepted by electrons in the material, and display a rough positive step function in energy at the bandgap. Photoluminescence measurements probe the energies of light emitted by these excited electrons after they have some time to settle in the conduction band. This means that photoluminescence data often looks like a sharp feature at the bandgap, but may extend into lower energies if excitons are present, as in the case of many perovskites. Figure from [2].

information to the perovskite community. When the electron and hole are in proximity to each other, they lower each other's potential energy in comparison to the default bandgap energy due to Coulomb attraction, which allows photoluminescence to be emitted at wavelengths longer than created by the bandgap. Exciton binding energy is the term for this energy change measured relative to the bandgap.

Excitons exhibit both a dipole moment and polarizability due to their nature of containing a positive and a negative charge with slight physical separation. They also have an effective mass and radius when treated as a particle similar to the hydrogen atom, but with an electron hole instead of proton. These values can be calculated from optical data and are interesting to the perovskite community, but have proven challenging to measure.

1.3 Benefits and requirements of the electroabsorption technique

Electroabsorption is a modification to the process of collecting absorption data that includes the addition of an alternating electrical signal across electrodes near the sample. When an electrical field is applied across the sample, the absorption will be altered due many effects, including the linear and quadratic Stark effects, that will shift or broaden optical features. When this electric field is modulated in time and the optical data interpreted by a lock-in amplifier, the resulting data is essentially the difference between the electrically-modified signal and the regular absorption signal, demonstrated in Fig. 1.4. The amplitude and shape of the electroabsorption features are related to many important parameters in perovskites and give a lot of insight on their internal structure and properties [1]. Additionally, in some perovskites where optical data would typically be obscured by disorder-induced peak broadening, this method potentially allows for very crisp measurements of optical features.

The extremely strong electric fields necessary for this experiment can be created in a sample by generating high voltages in close proximity to each other, since $E = V/d$ in free space. We use a configuration called interdigitated electrodes (IDEs), which consist of alternating rows of electrode fingers with only a few microns of separation, creating very strong electric fields between them over most of the perovskite film, which is deposited on top. A more detailed description of IDEs is given in the second chapter of this thesis, and our process of creating them is described in the fourth chapter.

One issue with calculating certain sample parameters from electroabsorption peaks is that it requires knowledge of the precise electric field strength. Although this may be estimated from $E = V/d$ in free space, it is not correct in general because it does not account for the response of the material to the applied electric field. If the material has any significant dielectric constant, then

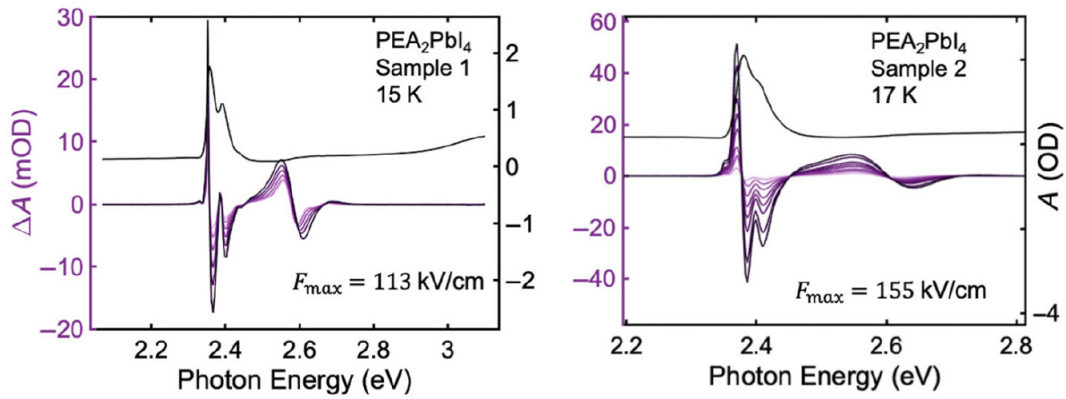


Figure 1.4 Plots demonstrating the relationship between absorption spectra (black, right axes) and electroabsorption spectra (purple, left axes) on two different PEPI perovskite samples. Electroabsorption is the difference between absorption data with an applied electric field, which may shift or broaden absorption features, and without an applied field. The way these features scale with electric field strength provides data on several important characteristics of the excitons that create them. Figure from [1].

it will set up its own internal electrical field in opposition to the applied field, so the net electric field in the sample will be reduced. It therefore becomes essential to know the material's dielectric constant in order to deduce the net electric field in the sample for the calculations described above. Unfortunately, this is not always simple to do.

1.4 The absence of permittivity data on perovskites

Dielectric constant ϵ_r , or relative permittivity (relative to the vacuum permittivity ϵ_0), is a value that describes the way matter interacts with electromagnetic waves, which varies with the frequency of applied electric field. At low frequencies (below 10^{10} Hz), measurements are often generated by an AC electrical signal using radio or microwaves. When frequency increases by a few more orders of magnitude, the electric field frequency becomes that of visible light, and then optical experiments can be done to measure the dielectric constant. Dielectric constant is related to index of refraction by a square root: $n = \sqrt{\epsilon_r}$.

The Lorentz oscillator model describes how the dielectric constant of a material varies with frequency. There are several physical modes that can contribute to a material's ability to oppose an electric field, but these modes become active at different time scales. Working from fast-acting high frequency responses to slower low-frequency responses, the dielectric constant increases in a step-like manner whenever any of these modes are reached, as detailed in Fig. 1.5. First, at frequencies between 10^{14} and 10^{16} Hz (each period lasting between 0.1 and 10 femtoseconds), the only mechanism fast enough to respond is the shape of the electron cloud around each atom: the negative cloud is distorted slightly towards the positive potential, creating a dipole. Next, at frequencies near 10^{13} Hz (on the scale of 0.1 picoseconds), the bonds between ions in the crystalline lattice can contract and expand in a spring-like motion, changing the polarization. Last, at frequencies near 10^9 Hz (on the scale of 1 nanosecond), any large molecules with a net dipole moment in the films may rotate into alignment with the field to reduce their potential energy, which further increases the polarization of the material.

In liquids, there is another potential mode that can become active at frequencies below 1 kHz (period larger than about 1 millisecond), called the diffusional mode. Here, ions and molecules with net charge in the liquid will be pulled towards either electrode due to the electric potential generated, which creates a charge separation and therefore a net dipole with polarization. The lower the frequency, the longer amount of time this effect has to take place, and as such, extremely large dielectric constants can exist at low frequencies in fluids.

Surprisingly, perovskite materials are believed to have a diffusional response as well, even though they are solids [5]. This implies that the atoms are actually swapping places within the crystalline lattice, a characteristic called "ion migration" that was controversial in the scientific community until recently. As such, perovskite materials have been described as potentially showing a huge increase in dielectric constant at frequencies below about 1 kHz. This happens to be near the frequency of interest that we use for electroabsorption in our laboratory, as do many others, so there

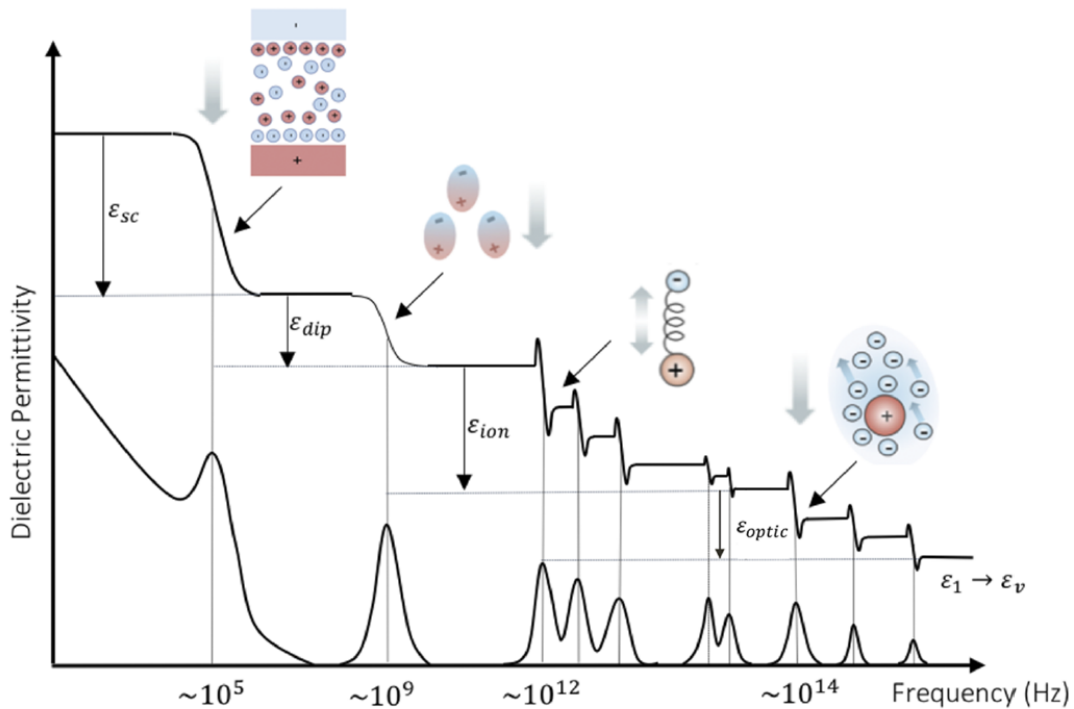


Figure 1.5 Diagram of the complex dielectric function of perovskites, as explained by the Lorentz oscillator model. The Lorentz oscillator model describes how various polarization mechanisms affect a material's ability to respond to an applied electric field in various time regimes. At high optical frequencies, only the fastest mechanisms like electron cloud distortion are able to respond to the field before it switches direction, but at low frequencies there are impacts from most mechanisms including atomic bond motion, molecular dipole alignment, and space charge migration. Figure from [4].

exists a need to better understand the behavior of the dielectric constant of perovskites within this frequency range.

Though there have been many measurements of perovskites at microwave frequencies and above, there are remarkably few reported values in the low-frequency range. Lin *et al.* predict a relatively stable dielectric constant for MAPI near $\epsilon_r = 35.19$ for frequencies between 100 Hz and 100 kHz [6], while Anusca *et al.* measure values near $\epsilon_r = 63.10$ above 100 kHz, with the dielectric constant increasing dramatically at lower frequencies [5]. Juarez-Perez *et al.* corroborate the existence of extremely high dielectric constant values at low frequency, reporting a static value on the order of $\epsilon_r = 1000$ [7]. There has also been one ϵ_∞ measurement on PEPI by Hong *et al.* in the low frequency range, with a reported value of $\epsilon_\infty = 4.41$ [8], but there are no published low frequency spectra on PEPI.

The goal of this thesis is to acquire measurements of the dielectric constant of perovskite thin films in this low-frequency range, from 5 Hz to 13 MHz. As may be indicated by the lack of measurements in this range in the scientific community thus far, this is more challenging to do than one might think. We will attempt to use impedance data collected on our perovskite films measured within this frequency range to calculate permittivity values that would explain these impedance measurements.

1.5 Relationship between permittivity and capacitance

Permittivity is highly related to capacitance. While permittivity is a property intrinsic to materials, capacitance is a measured quantity that describes a system's ability to store charge in response to an electric potential. This will include contributions from a material's permittivity, but is also impacted by the physical geometry of the system. The larger a material's permittivity, the larger its capacitance measurement becomes because a stronger internal electric field is generated in the

material, which is able to store more energy.

Given this strong relationship, it makes sense that one should be able to relate these quantities mathematically. Since capacitance is easily measurable, it is plausible to be able to find a mathematical equation that relates capacitance to permittivity, if one has information on the geometrical configuration of the system. For something as classic as the parallel-plate capacitor configuration, the geometric factor depends only on the ratio of the plate area to their separation: $C = \frac{\epsilon_0 \epsilon_r A}{d}$. However, if we need to create a model based on a more complicated electrode configuration, such as the IDEs required for electroabsorption, the geometric factor quickly becomes extremely complicated. Chapter 2 details the mathematical process of relating capacitance to permittivity in the case of IDEs.

Additionally, permittivity is a complex quantity, and the imaginary part is related to the material's resistance and conductance. Although my work does not focus on this aspect of permittivity at this point, it could be useful in the future, so data is collected on both capacitance and resistance, i.e. the total impedance vector. We measure the magnitudes of Z, R, and C at each frequency point.

1.6 Parallel plate electrode geometries

As mentioned in the previous section, one of the most common methods of measuring the complex permittivity of perovskites and similar materials is via impedance measurements on a parallel plate electrode apparatus. Parallel plate electrodes allow a relatively uniform and linear electric field to be constructed between them, which a dielectric material can respond to evenly according to $C = \frac{\epsilon_0 \epsilon_r A}{d}$.

Nearly all low-frequency complex impedance measurements are acquired using impedance analyzer machines specifically created for this task. They are capable of measuring the magnitudes of resistance, capacitance, inductance, overall impedance, and more using a coaxial input that can be connected to electrodes. They generate AC frequencies for the material to respond to, and can

record data on computers with appropriate drivers and software.

There are a few methods available to create the parallel plate electrode geometry for their impedance measurements. Some of the impedance analyzer machines have attachable parallel plate fixtures for this purpose. They have metal plates with micrometer-adjustable plate separation and several methods to calibrate the measurements they give on the impedance analyzer. A sample can be placed between the plates, its impedance spectrum measured, and then its dielectric function calculated based on the plate area and separation.

While use of this fixture is convenient and requires only simple equations to compute dielectric function, it can be insensitive to small samples like thin films, especially if they are attached to a substrate. We attempted to use such an apparatus with perovskite samples, both as thin films grown on a substrate and as crystals pressed into flat pellets.

We obtained a series of dielectric function measurements on PEPI in pressed pellet form that are in agreement with the static value presented by Hong *et al.* [8], presented in Fig. 1.6. However, there were substantial issues in the calibration process as well as with the precision of these measurements, and we saw large variability whenever the fixture was adjusted. While the data from these measurements are acceptable, it is nearly impossible to create large enough pellets from most other types of perovskites we are interested in measuring, so this method was abandoned.

With modifications to the parallel plate capacitor equation, dielectric functions could in theory be calculated from samples on a substrate, as long as the thickness of each part is known. However, we were never able to obtain reasonable values, since the extreme thinness of the perovskite thin films amplified all the error in these measurements. This method was deemed impractical, and abandoned as well.

An alternative way to use parallel plate geometry is to deposit or paste metal electrodes directly onto the sample instead of placing the sample inside a rigid fixture. When using pasted electrodes, as long as the thickness of the sample can be determined, then there are no additional complexities

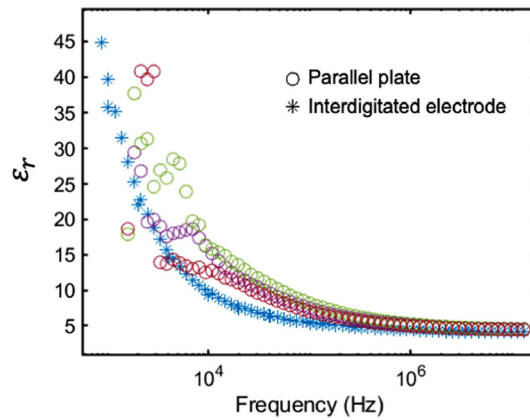


Figure 1.6 Our calculations of the dielectric function of PEPI, where circles indicate measurements using pressed pellets in a parallel plate electrode fixture, and stars represent measurements from thin films grown on IDEs. Figure from [1].

in accounting for air gaps or sample substrates in the parallel plate capacitor equation.

One example of this method's use is described in a manuscript by Anusca *et al.*, in which experimental data of complex permittivity for MAPI and MAPbBr₃ (MAPBr) are provided for frequencies below 1 MHz [5]. They grew crystals of each material and pressed them into flat pellets that would fit the shape of parallel plate electrodes. They further ensured flat surfaces by polishing the surfaces of the pellets and washing them in acetone to eliminate roughness. Then, they were able to paint electrodes onto either side of the pellets using silver paste and measure complex impedance across the perovskite pellets. Lin *et al.* report reasonably similar values for MAPI, using the same technique to generate the real dielectric function, and using CELIV, a method of measuring current densities, to generate the imaginary dielectric function [6].

There are many obvious benefits to using a parallel electrode geometry. It is relatively simple to calculate dielectric function mathematically in this geometry since the applied electric field is uniform and linear. If the sample can be grown in large enough sizes to produce reasonably thick films or pellets, then this method may be sufficient to determine the complex permittivity. Because of its ease, two of the three perovskite measurements that have been published so far have been

done using this technique.

However, since not all of our materials can be grown in sufficient quantity to be pressed into thick pellets, there are many types of perovskites that we would be unable to measure. Additionally, many of our samples grow in alternating layers that create anisotropy in dielectric measurements of thin films. The dielectric measurements of a pressed pellet will lose any directional information present in the thin film and may provide incorrect values accordingly.

1.7 Adjacent electrode geometries

While there are many clear benefits to having a uniform and linear electric field as constructed between parallel plate electrodes, this element is not essential. As long as a mathematical relationship can be established between impedance measurements and complex permittivity, there are many potential electrode arrangements that can be investigated.

One such electrode arrangement is that of adjacent electrodes, deposited in the same horizontal plane. In this arrangement, rather than sandwiching the perovskite between electrodes, the perovskite is grown on top of them. The electric field lines arc from one electrode to the other on both sides, rather than pass between them linearly. The mathematical model for parallel plate capacitors can still be used with some accuracy in this case [9], surprisingly, but many choose to create a more descriptive geometrical model that can account for the different electric field line paths and strengths in the arcs. Torchyniuk *et al.* use a multi-step model with both a parallel plate component in-layer with the electrodes and arcing component on either side of the electrodes [10]. Since electric field lines may pass through one region or the other, this model is analogous to parallel circuit elements, where the capacitance of each region may be summed to find the total capacitance of the system.

Another electrode arrangement is that of the split ring resonator. Split ring resonators (SRRs) are arrays of concentric circular or rectangular rings, with gaps, that are typically used to modify

magnetic susceptibility in technological applications. However, Su *et al.* have demonstrated that this configuration of electrodes can also be used to obtain very sensitive measurements of the dielectric constants of fluids since it can support the application of an alternating current [11]. They find that studying the resonant frequencies of SRRs in liquids provides information about capacitance and therefore the dielectric constant of these liquids.

The various adjacent configurations of electrodes provide many advantages when compared to parallel electrodes, particularly in their ability to sense accurately at small scales, since the electric field lines are confined close to the electrode surfaces. IDEs are another type of configuration of adjacent electrodes placed on a surface, and as such they have the potential to allow highly accurate impedance measurements of perovskite thin films as long as an accurate mathematical model exists. That is the purpose of this thesis: to establish a mathematical relationship between the relative permittivity of perovskites and the overall capacitance across the IDE electrodes on which the perovskites are deposited, so that no other methods are required to measure their permittivity.

Chapter 2

Development of Mathematical Model

2.1 Interdigitated electrode geometries

The interdigitated electrode format is a patterned area of alternating stripes of electrodes. Every-other stripe/finger has opposite electric potential just a few microns apart, so very strong electric fields are generated near them. This electrode configuration is chosen for use in optical electroabsorption experiments precisely because of these strong electric fields, and because of their semi-transparency to light. Since IDEs fall into the category of adjacent electrodes described in Chapter 1, they create electric field lines that travel in both straight lines or arcs, depending on the region of space. A diagram of this electrode configuration and the electric field lines it generates is shown in Fig. 2.1.

It becomes significantly more challenging to create a mathematical model for this electrode arrangement than for simple adjacent or parallel plate electrodes. Many choose to use the parallel plate electrode model of capacitance even when using an IDE format, such as Gennaro *et al.* [12], Chen *et al.* [13], and Risos *et al.* [14], who successfully measured the dielectric constants of several materials. This is a very reasonable option, especially in the case of extremely thin films where the sample lies almost entirely between the electrode gaps where the electric field

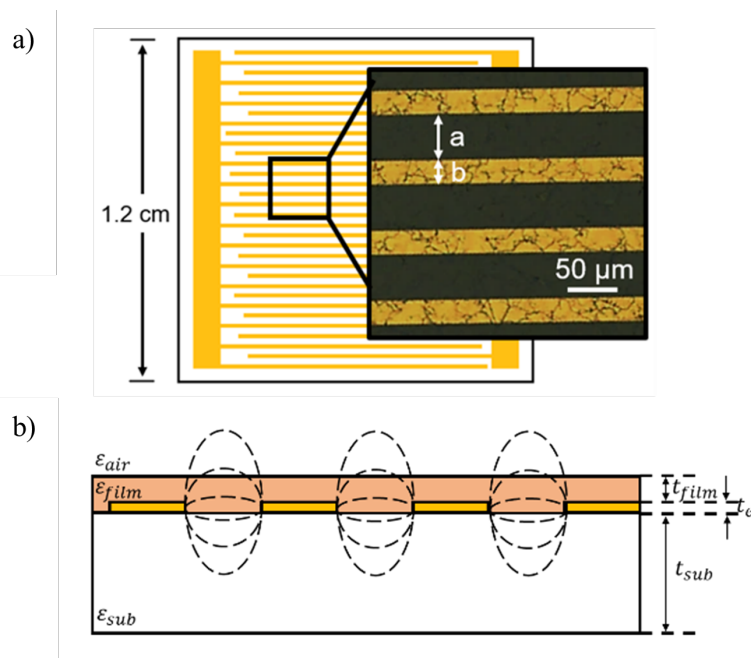


Figure 2.1 (a) Top-view diagram of gold interdigitated electrodes photolithographically deposited onto quartz substrate. (b) Side-view diagram of perovskite material grown on electrode substrates, with dashed lines representing electric field lines induced by an alternating signal.

follows straight lines [15]. In many cases this model is sufficient, but there has also been interest demonstrated by the scientific community in developing a more precise mathematical model for measurement of dielectric constants. Development of new measurement technique has been done both experimentally and computationally, as many have started to computationally model the dielectric constant of perovskites and similar films using various electrode geometries using finite element method [16–18].

A detailed approximation of capacitance from IDEs was made by Farnell *et al.* in 1970 [19]. The model accounts for the precise finger geometry and for the presence of a substrate, and appears to make accurate measurements. However, it does not allow for the presence of other layers of material, nor does it take anisotropy into account. Dimos *et al.* used this model to measure the permittivity of several materials as thin films deposited on a substrate [20]. We intend to create a new, more flexible model for capacitance from IDEs that will hopefully allow measurements with several materials and preserve directional information, although its development is not entirely finished at this point. While we compare our measurements of material's dielectric functions to those made in literature in Chapters 3 and 4, we are also interested in comparing the success of our model versus these other IDE models when using the same data set, so that their accuracy can be compared.

2.2 New approach to 3D interdigitated electrode model

In 1969, Helge Engan made another thorough mathematical analysis of the interdigitated electrode configuration in a manuscript that has been cited by many, introducing a mathematical model of capacitance for two materials [21]. However, as discussed in an article by Matthijs W. den Otter in 2001, the equations presented in Engan's article are difficult to solve [22], thus they would be challenging for our script to solve hundreds of times for data points in a large frequency spectrum.

As such, den Otter creates an approximation designed to imitate but simplify the solution by Engan; rather than considering the electric potential of the whole electrode geometry at once, den Otter ignores the effects of charge from fingers that are far away, and then represents this approximation over all space using a periodic Fourier series expansion. By relating the energy stored within the electric fields described by the model to the energy stored in a general capacitor, one can relate the dielectric constant of nearby material to the overall capacitance of the electrodes. This greatly simplifies the equations yet den Otter shows that it holds as an extremely close approximation as long as the finger width-to-period ratio remains between 0.2 and 0.85 [22]. In addition, den Otter's equations have clear spatial dependence in three dimensions, which allows them to be easily altered to consider more layers of materials, whereas Engan's have no clear spatial relation other than through two spatial boundary conditions.

We saw the potential to adapt this model to determine the dielectric of perovskite thin films on quartz substrates. However, there were some modifications that we needed to make to fit our configuration, and there will be more modifications in the future to preserve the anisotropic nature of the dielectric constant.

2.3 The mathematical model for capacitance

As it stands, den Otter's model considers IDEs in plain air with no surrounding materials. This is definitely not the case for our perovskite thin films deposited on quartz. We needed to alter this model to include different dielectric constants in different relative thicknesses, and at different distances from the electrodes, which are all factors that influence the strength of the electric field. The coordinate system and variables that we will be using are shown in Fig. 2.2.

Since electric potential V is constant along the length of the electrodes, the solutions to the

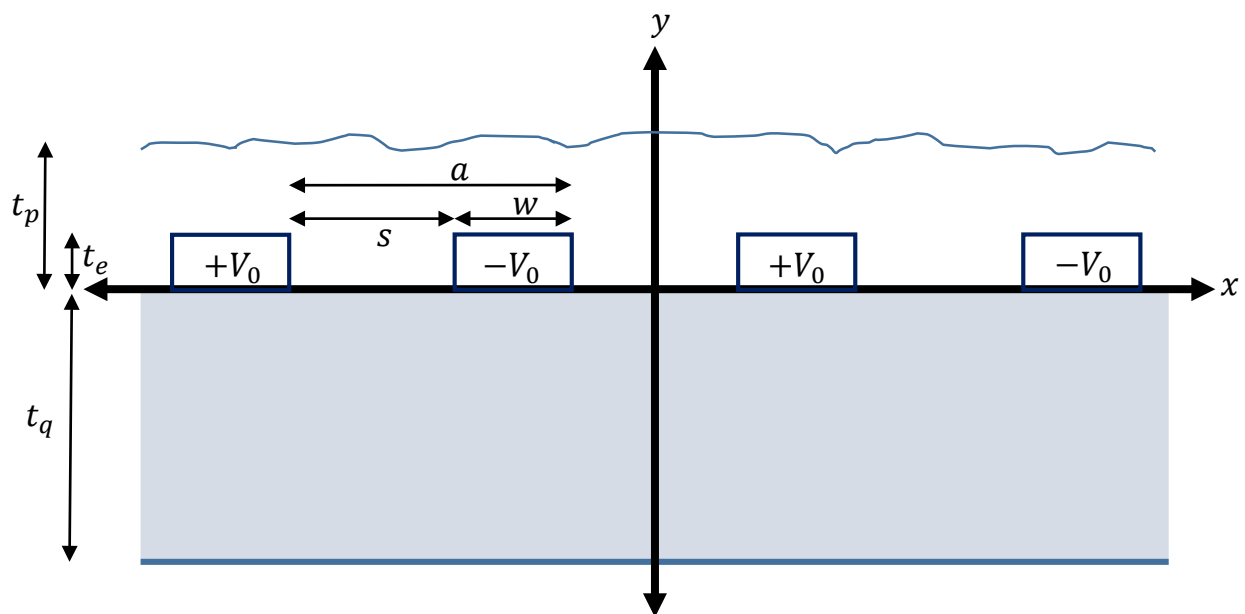


Figure 2.2 Diagram of the variables used in the mathematical model, adapted from the work of den Otter [22]. Variables a , s , and w describe the periodic pattern of the fingers, variables t_p , t_e , and t_q represent material thicknesses, and V_0 represents the electric potential generated. Not depicted are variables q and p , which represent the total area over which the IDEs span in the x and z coordinates, respectively.

separable 2D Laplace equation in the x - y plane indicate equations of this general form:

$$V(x,y) = \sin\left(\frac{(2n-1)\pi x}{a}\right) \exp\left(-\frac{(2n-1)\pi|y|}{a}\right) \quad (2.1)$$

The potential oscillates when one moves across the surface of the IDE in the x direction, and decays with distance in the y direction.

Next, we follow den Otter's example by fitting the electric potential equation to the specific geometry of our system and to the established decay function in space [23], using a Fourier coefficient expansion of harmonics. The result of this is

$$V(x,y) = \sum_{n=1}^{\infty} B_n \sin\left(\frac{(2n-1)\pi x}{a}\right) \exp\left(-\frac{(2n-1)\pi|y|}{a}\right), \quad (2.2)$$

with

$$B_n = \frac{4V_0}{(2n-1)\pi} J_0\left(\frac{(2n-1)\pi s}{2a}\right).$$

This potential shape in space is demonstrated in Fig. 2.3 where potential is plotted against x and z position. The square of the slope of this surface is proportional to the amount of energy that is stored in the electric field at that location.

Since we must know the electric field \mathbf{E} to calculate the energy, we may use the gradient to determine \mathbf{E} according to the equation $\mathbf{E} = -\nabla V$. Then, we find that for $y > 0$,

$$\mathbf{E} = \sum_{n=1}^{\infty} B_n \frac{(2n-1)\pi}{a} \exp\left(-\frac{(2n-1)\pi y}{a}\right) \left[\cos\left(\frac{(2n-1)\pi x}{a}\right) \hat{\mathbf{x}} - \sin\left(\frac{(2n-1)\pi x}{a}\right) \hat{\mathbf{y}} \right] \quad (2.3)$$

and for $y < 0$,

$$\mathbf{E} = \sum_{n=1}^{\infty} B_n \frac{(2n-1)\pi}{a} \exp\left(\frac{(2n-1)\pi y}{a}\right) \left[\cos\left(\frac{(2n-1)\pi x}{a}\right) \hat{\mathbf{x}} + \sin\left(\frac{(2n-1)\pi x}{a}\right) \hat{\mathbf{y}} \right]. \quad (2.4)$$

den Otter integrates the field-strength decay equation over all space using just one dielectric constant. However, if we split the integral over the y -axis into separate integrals over various distance regions, then we can add layers of different materials to the model. By considering the dielectric constant of quartz below the electrodes (from $t = -t_q$ to $t = 0$ in an arcing region), the

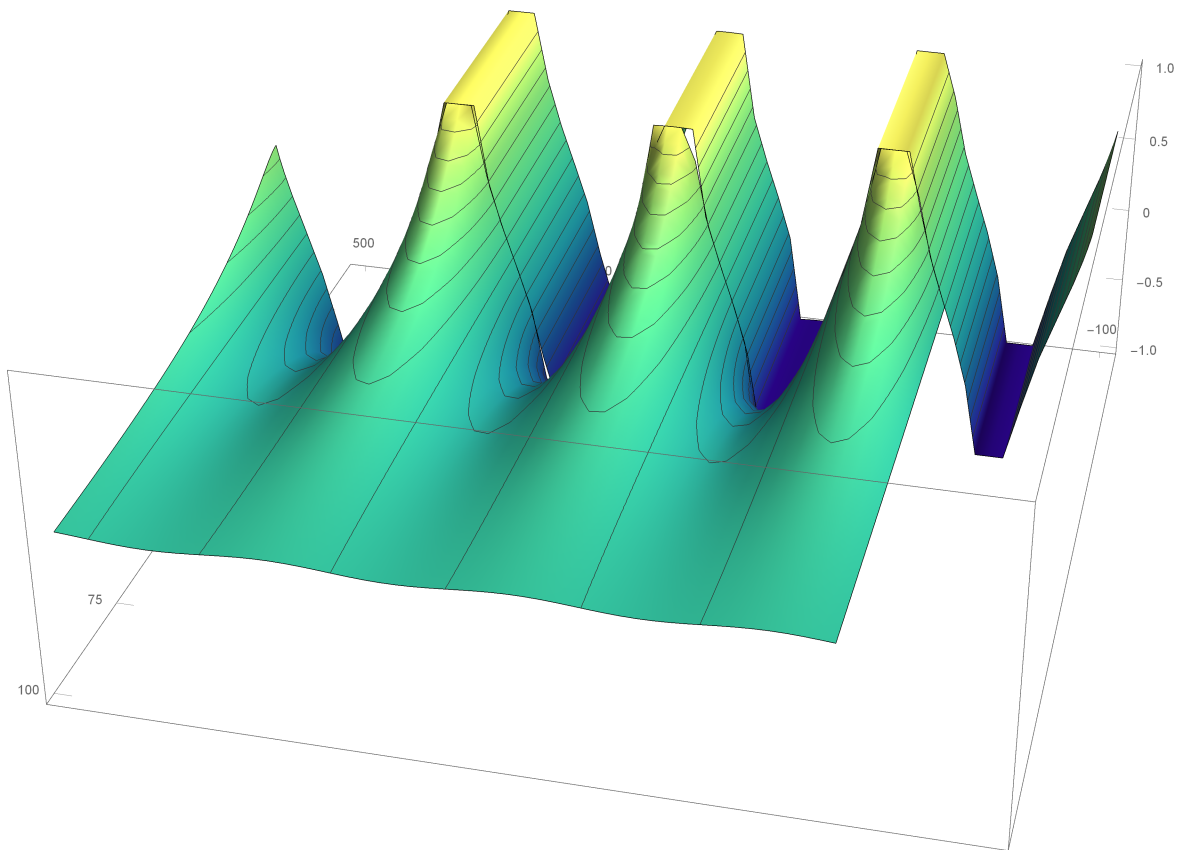


Figure 2.3 Plots of electric potential versus position across and away from the electrodes. Between the electrodes the potential is linear due to constant electric field, and these values decay with distance from the electrode.

variable dielectric constant of perovskite in question (from $t = 0$ to $t = t_e$ in a near constant field region, see next paragraph, and from $t = t_e$ to $t = t_p$ in an arcing region), and the dielectric constant of air both above and below these layers (from $t = -\infty$ to $t = -t_q$ and from $t = t_p$ to $t = \infty$, both in arcing regions), each section's overall impact on the capacitance will be included. Then, by setting the overall energy stored in these electric field regions ($U = \frac{1}{2} \int \mathbf{D} \cdot \mathbf{E} dV$) equal to the energy stored in a capacitor, ($U = \frac{1}{2} CV^2$), the relationship between capacitance and various dielectric constants is determined. We solve equations of this form for blank substrates and for perovskite samples, which require different equations because they involve different layers of materials.

Since the thickness of the electrodes is on the same order of magnitude of the thickness of some of our thin films, we included in our model a contribution from an inside-electrode-region that behaves slightly differently than the surrounding arcing regions. Within the electrode thickness, the electric field does not decay along the y -axis and can be approximated as a nearly constant field. To do this we took the potential function in the $y = 0$ plane from den Otter's model and extended it from $y = 0$ to $y = t_e$. The surrounding region distances were carefully shifted in the calculations as to not double count any region of material.

One could also easily approximate this area as a parallel plate electrode winding through the IDE gap due to the presence of uniform field. When this approximation is used, the capacitance value generated is extremely similar to the capacitance value generated by the extension of the $y = 0$ plane, which assures us that the calculations are robust.

For the blank IDEs, we find that (using k to represent dielectric constant for simplicity):

$$\begin{aligned}
\frac{1}{2}C_0(2V_0)^2pq &= \frac{\epsilon_0}{2} \int_0^q dx \int_0^p dz \left[k_{air} \int_{-\infty}^{-t_q} \left(\left(\sum_{n=1}^{\infty} B_n \frac{(2n-1)\pi}{a} \exp\left(\frac{(2n-1)\pi y}{a}\right) \cos\left(\frac{(2n-1)\pi x}{a}\right) \right)^2 \right. \right. \\
&\quad \left. \left. + \left(\sum_{n=1}^{\infty} B_n \frac{(2n-1)\pi}{a} \exp\left(\frac{(2n-1)\pi y}{a}\right) \sin\left(\frac{(2n-1)\pi x}{a}\right) \right)^2 \right) dy \right. \\
&\quad \left. + k_Q \int_{-t_q}^0 \left(\left(\sum_{n=1}^{\infty} B_n \frac{(2n-1)\pi}{a} \exp\left(\frac{(2n-1)\pi y}{a}\right) \cos\left(\frac{(2n-1)\pi x}{a}\right) \right)^2 \right. \right. \\
&\quad \left. \left. + \left(\sum_{n=1}^{\infty} B_n \frac{(2n-1)\pi}{a} \exp\left(\frac{(2n-1)\pi y}{a}\right) \sin\left(\frac{(2n-1)\pi x}{a}\right) \right)^2 \right) dy \right. \\
&\quad \left. + k_{air} \int_0^{t_e} \left(\sum_{n=1}^{\infty} B_n \frac{(2n-1)\pi}{a} \cos\left(\frac{(2n-1)\pi x}{a}\right) \right)^2 dy \right. \\
&\quad \left. + k_{air} \int_{t_e}^{\infty} \left(\left(\sum_{n=1}^{\infty} B_n \frac{(2n-1)\pi}{a} \exp\left(-\frac{(2n-1)\pi y}{a}\right) \cos\left(\frac{(2n-1)\pi x}{a}\right) \right)^2 \right. \right. \\
&\quad \left. \left. + \left(\sum_{n=1}^{\infty} B_n \frac{(2n-1)\pi}{a} \exp\left(-\frac{(2n-1)\pi y}{a}\right) \sin\left(\frac{(2n-1)\pi x}{a}\right) \right)^2 \right) dy \right]. \tag{2.5}
\end{aligned}$$

We can then solve for the capacitance C from the blank in terms of each layer's dielectric constant, thickness, and location:

$$\begin{aligned}
C_{quartz} &= \frac{\epsilon_0 pq}{a} \left(\frac{\pi}{8V_0^2} \sum_{n=1}^{\infty} B_n^2 \left[\left(k_{air}(1) + k_{air} \exp\left(-\frac{2(2n-1)\pi t_q}{a}\right) \right) \right. \right. \\
&\quad \left. \left. + k_Q \left(1 - \exp\left(-\frac{2(2n-1)\pi t_q}{a}\right) \right) \right] (2n-1) \right. \\
&\quad \left. \left. + \left(k_{air} \left(\frac{t_e \pi}{a} \right) \right) (2n-1)^2 \right] \right). \tag{2.6}
\end{aligned}$$

Obtaining this equation allows us to relate our measured capacitance values of the blank substrate IDEs to the dielectric constant of quartz. We will need to know the dielectric function of quartz in Eq. 2.7 in order to obtain the dielectric function of the perovskite thin film, otherwise there would be too many variables to solve for in the system.

Next, we repeat the same process for the perovskite sample by adding additional material regions above the IDEs:

$$\begin{aligned}
\frac{1}{2}C_0(2V_0)^2pq = & \frac{\epsilon_0}{2} \int_0^q dx \int_0^p dz \left[k_{air} \int_{-\infty}^{-t_q} \left(\left(\sum_{n=1}^{\infty} B_n \frac{(2n-1)\pi}{a} \exp\left(\frac{(2n-1)\pi y}{a}\right) \cos\left(\frac{(2n-1)\pi x}{a}\right) \right)^2 \right. \right. \\
& + \left. \left(\sum_{n=1}^{\infty} B_n \frac{(2n-1)\pi}{a} \exp\left(\frac{(2n-1)\pi y}{a}\right) \sin\left(\frac{(2n-1)\pi x}{a}\right) \right)^2 \right) dy \\
& + k_Q \int_{-t_q}^0 \left(\left(\sum_{n=1}^{\infty} B_n \frac{(2n-1)\pi}{a} \exp\left(\frac{(2n-1)\pi y}{a}\right) \cos\left(\frac{(2n-1)\pi x}{a}\right) \right)^2 \right. \\
& + \left. \left(\sum_{n=1}^{\infty} B_n \frac{(2n-1)\pi}{a} \exp\left(\frac{(2n-1)\pi y}{a}\right) \sin\left(\frac{(2n-1)\pi x}{a}\right) \right)^2 \right) dy \\
& + k_P \int_0^{t_e} \left(\sum_{n=1}^{\infty} B_n \frac{(2n-1)\pi}{a} \cos\left(\frac{(2n-1)\pi x}{a}\right) \right)^2 dy \\
& + k_P \int_{t_e}^{t_p} \left(\left(\sum_{n=1}^{\infty} B_n \frac{(2n-1)\pi}{a} \exp\left(-\frac{(2n-1)\pi y}{a}\right) \cos\left(\frac{(2n-1)\pi x}{a}\right) \right)^2 \right. \\
& + \left. \left(\sum_{n=1}^{\infty} B_n \frac{(2n-1)\pi}{a} \exp\left(-\frac{(2n-1)\pi y}{a}\right) \sin\left(\frac{(2n-1)\pi x}{a}\right) \right)^2 \right) dy \\
& + k_{air} \int_{t_p}^{\infty} \left(\left(\sum_{n=1}^{\infty} B_n \frac{(2n-1)\pi}{a} \exp\left(-\frac{(2n-1)\pi y}{a}\right) \cos\left(\frac{(2n-1)\pi x}{a}\right) \right)^2 \right. \\
& + \left. \left(\sum_{n=1}^{\infty} B_n \frac{(2n-1)\pi}{a} \exp\left(-\frac{(2n-1)\pi y}{a}\right) \sin\left(\frac{(2n-1)\pi x}{a}\right) \right)^2 \right) dy \left. \right]
\end{aligned} \tag{2.7}$$

Then, we are able to solve for the new overall capacitance of the perovskite samples on IDE substrate, in terms of the unknown dielectric constant of the perovskite film, and the known dielectric constants of air and quartz, as well as the known geometrical parameters.

$$\begin{aligned}
C_P = \frac{\epsilon_0 p q}{a} \left(\frac{\pi}{8V_0^2} \sum_{n=1}^{\infty} B_n^2 \left[\left(k_{air} \exp \left(-\frac{2(2n-1)\pi(t_p-t_e)}{a} \right) + k_{air} \exp \left(-\frac{2(2n-1)\pi t_q}{a} \right) \right. \right. \right. \\
\left. \left. \left. + k_Q \left(1 - \exp \left(-\frac{2(2n-1)\pi t_q}{a} \right) \right) + k_P \left(1 - \exp \left(-\frac{2(2n-1)\pi(t_p-t_e)}{a} \right) \right) \right] (2n-1) \right. \\
\left. \left. \left. + \left(k_P \left(\frac{t_e \pi}{a} \right) \right) (2n-1)^2 \right] \right). \quad (2.8)
\end{aligned}$$

Now, the modifications to den Otter's model allow us to add several materials and tune their thicknesses to fit the geometry of our perovskite samples. It also opens the door to consider the effect of anisotropy in dielectric constant in the future, since the equations can be modified to work in three dimensions using a dielectric constant tensor.

Chapters 3 and 4 in this thesis present dielectric functions of several materials that were calculated using this adapted model of den Otter, and compare their results to other measurements in literature.

Chapter 3

Testing Model on Quartz and Water

3.1 Measurements on quartz substrate

The first step required to calculate the dielectric constant of perovskite thin films using our model is to measure the capacitance of the blank substrate with no thin film deposited. This allows us to calculate the dielectric function of quartz using Eq. 2.6, to allow its use in Eq. 2.8 and in testing the accuracy of the model. The results of solving Eq. 2.6 for the dielectric function of quartz using capacitance measurements from four different blank substrates, as well as one with higher averaging, are plotted in Fig. 3.1. We report values near 4.8 for frequencies above 100 Hz, with an increase below this frequency. There is great consistency between blank substrates.

Published dielectric constant values for quartz, reported by Krupka *et al.* [24] and De *et al.* [25], are overlaid with a closer view of our quartz measurements, in Fig. 3.2. In microwave-range frequencies, there are many published measurements of the dielectric constant of quartz that are in good agreement with each other. However, at sub-microwave frequencies, there are fewer reported measurements, and their values still have substantial disagreement. Our reported value of $\epsilon_r = 4.805$ seems slightly large when compared to the values reported by Krupka *et al.* [24], but

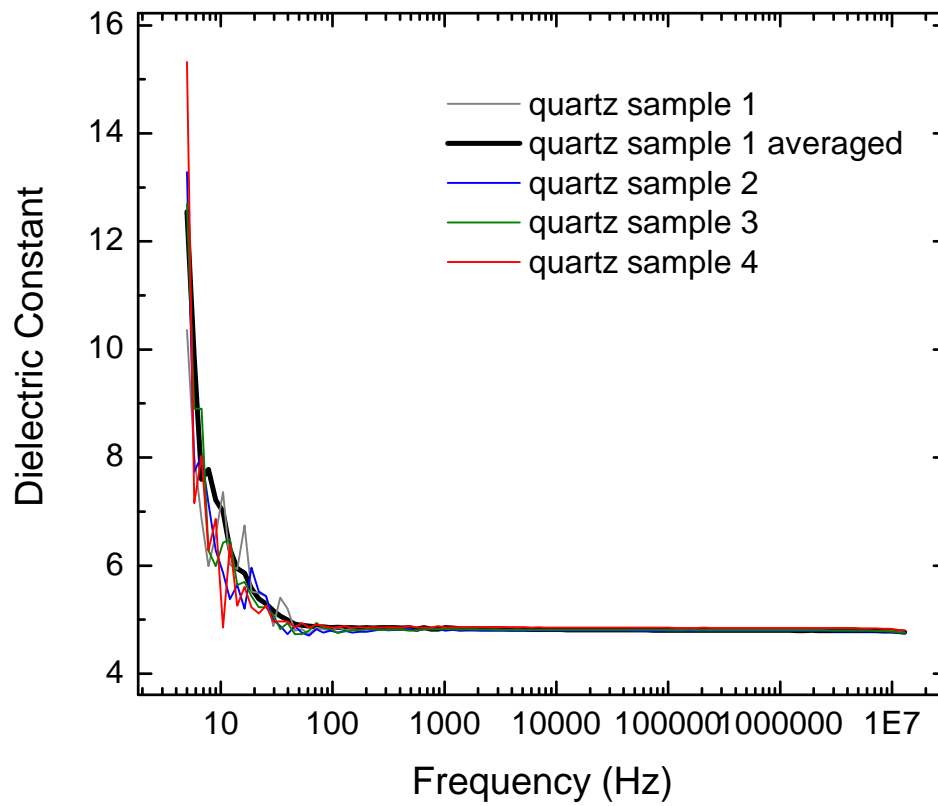


Figure 3.1 Calculated dielectric functions of quartz, measured from four different blank IDE substrates. Thin lines represent the four blank measurements, while the thick line represents a re-measurement of the first substrate, with 36 times more averaging.

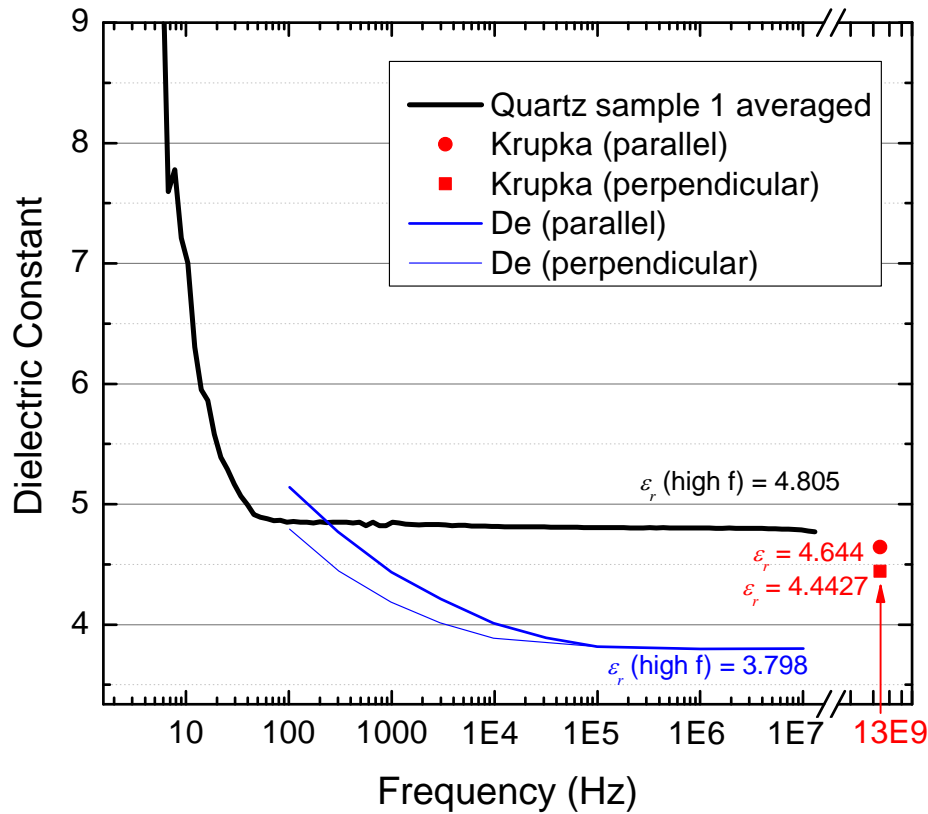


Figure 3.2 A closer view of our calculated dielectric functions of quartz, shown in black. The blue line represents measurements of quartz by De *et. al.* [25], and the red lines represent the parallel and perpendicular dielectric components of quartz measured by Krupka *et. al.* [24] at a much higher frequency value. There is moderate agreement between the values our model predicts and the published values, despite no overall consensus on the onset of the low-frequency dispersion.

the discrepancy could be due to the difference in measurement frequency, as the Lorentz model dictates that dielectric constant typically decreases with increasing frequency. Our measurements are larger than the measurements reported by De *et al.* [25] even in the same frequency range, but their measurements, as reflected in Fig. 3.2, are lower than one may expect considering its misfit with most accepted high frequency values.

Note that quartz displays two different dielectric constants depending on which direction through the crystalline lattice the electric field runs. When the electric field is parallel to the optically-defined z -axis, which runs perpendicular to the substrate surface of z -cut quartz, it is influenced by the parallel dielectric constant. When the electric field runs along the surface of the substrate, it is influenced by the perpendicular dielectric constant. The commonly accepted values of these parameters in quartz, given by Krupka *et. al.* [24], are $\epsilon_{r, parallel} = 4.6440$ and $\epsilon_{r, perpendicular} = 4.4427$. Since our electric fields travel in arcs between the electrode fingers, there is likely a contribution from each of these directions in what we measure. Because of this, it will be challenging to assign a number to precisely describe our error until the anisotropy-inclusive model is fully developed.

Overall, the measurements we have produced seem to agree reasonably well with accepted values, but may over-predict slightly. This may be a good indication that the model is able to provide a great estimate of the dielectric constant of materials in the vicinity of IDEs. Next we will perform another test on the model by calculating the well-studied dielectric function of water.

3.2 Measurements on water

Capacitance measurements on the IDEs with water in the vicinity were performed two ways: by placing the surface of the electrodes onto the top of a dish of ultra-pure water, and by immersing the electrodes completely. This requires the formation of two new equations from the model which are not shown, but create separate results that can be compared against each other.

The values we report are shown in Fig. 3.3. The two ways that water was measured yield values in close agreement with each other despite having significantly different capacitance equations, which is a good indication of consistency. The two high-frequency measurements of water's dielectric constant we acquired are $\epsilon_r = 84.318$ and $\epsilon_r = 83.105$, both slightly larger than the

expected value of $\epsilon_r = 80.054$ according to Batalioto *et al.* [26] and many others.

There is a discrepancy indicated between the reported values of Batalioto *et al.* [26] and that of Sherman *et al.* [27] below 10 kHz, relating to the onset of dispersion. This is most likely tied to the presence of other compounds in the water influencing the electrical signal measurements. The onset of the increase of dielectric constant occurring at higher frequencies (as frequency is reduced) most likely indicates less pure water, as there are more contaminants that can respond to the electrical signal.

Fig. 3.4 shows a closer look at frequencies above 10 kHz, where our high-frequency measurements can be more easily compared to values from Batalioto *et al.* [26].

Overall, the measurements of dielectric functions of quartz and of water can be good indicators of the success of the model, since their dielectric constants are known at certain frequencies. We see good agreement in the model presented in this thesis with these known values, finding an average error of 5.568% as an over prediction. Even with error, it will be useful to be able to estimate the rough values of dielectric constant on many perovskite films because there are no existing values in literature.

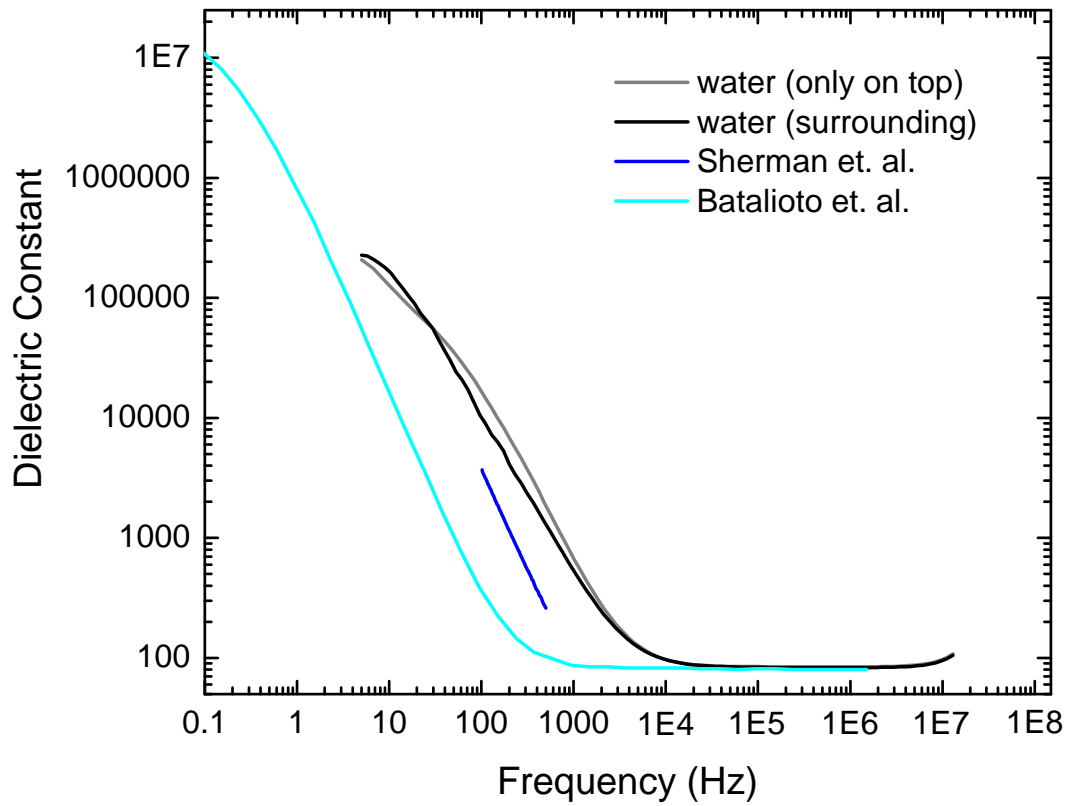


Figure 3.3 Two calculated dielectric functions for water are shown in black and gray. Data taken from Batalioto *et al.* [26] and Sherman *et al.* [27] are depicted in aqua and blue respectively for comparison.

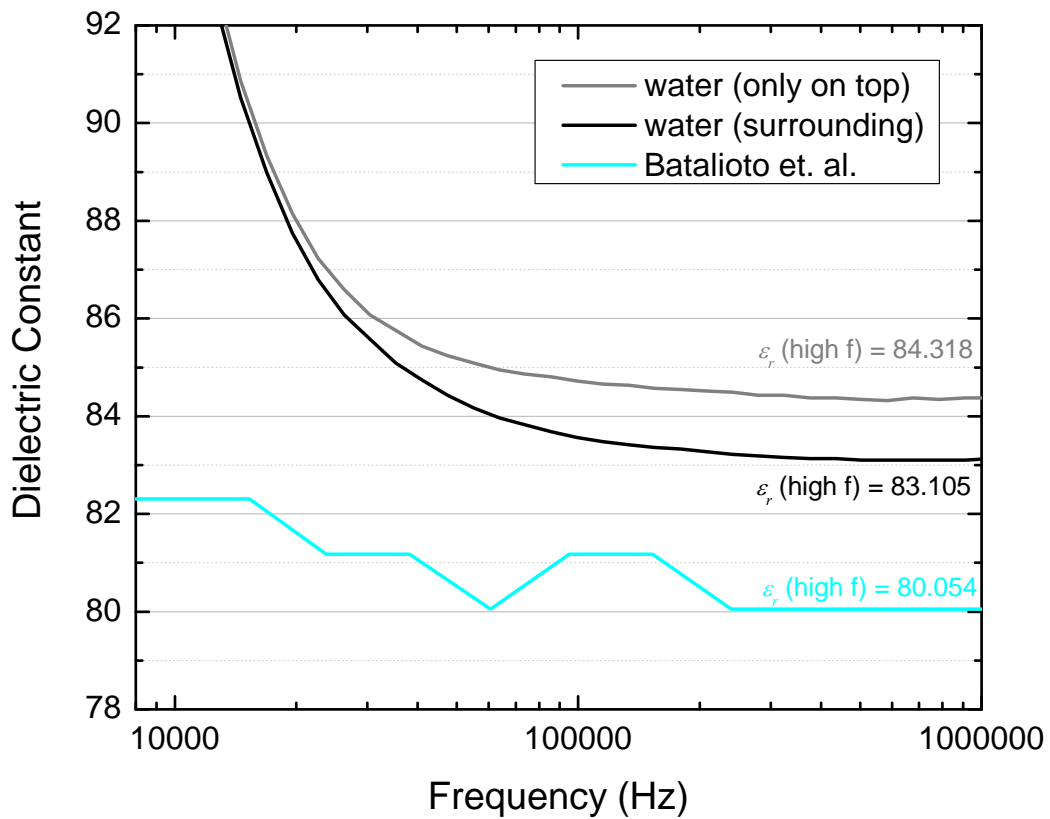


Figure 3.4 A closer view of the calculated dielectric functions for water are shown at frequencies above 10 kHz. The measurement by Batalioto *et al.* [26] is shown in blue.

Chapter 4

Dielectric Constant Measurements on Perovskites

4.1 Sample preparation on electrodes

Interdigitated electrode substrates are created at the Nano Fabrication Lab at the University of Utah from high quality z-cut 500 μm thick quartz wafers. The interdigitated electrode layout is created by photolithographically depositing an approximately 100 nm thick gold pattern onto the quartz wafer. The pattern, demonstrated in Fig. 2.1(a), consists of two long rectangular electrodes on opposite edges of the substrate, with many narrow (45 μm) fingers spanning the area between them. Each finger alternates connecting to the left or right edge-electrodes. The perovskite materials are then grown directly on top of the electrode array with thicknesses ranging from approximately 200 nm to 2.5 μm , depending on the specific sample. The close proximity of each alternating finger allows an alternating electrical signal to produce an extremely strong electric field between them. These electric fields are generated from charges on the surfaces of the electrodes, arcing from one to the next, and reach several microns deep into the materials on either side, shown in Fig. 2.1(b). This

means that the electrical response of both the substrate and perovskite film to the field will influence the overall impedance across the side electrodes.

To test the accuracy of the mathematical model in calculating the dielectric constant frequency spectrum of various materials, four blank substrates and 16 perovskite samples were prepared. The blank substrate measurements in Chapter 3 serve several purposes: to measure the dielectric spectrum of the quartz they were deposited on, and for use inside Eq. 2.8. Four types of perovskite thin films, PEPI, MAPI, PEAPbCl₄ (PEPCL) and PEAPbBr₄ (PEPBr), were deposited on IDE substrates by graduate student Kameron Hansen at the University of Utah. These specific types of perovskite films were selected because they are of interest in ongoing electroabsorption experiments. The duplicates of each measurement were intended to check the consistency of dielectric measurements.

Impedance measurements were collected using a commercial impedance analyzer for each sample at 101 data points between 5 Hz and 13 MHz on a logarithmic scale. Eight averages were done on the lowest 30 points to eliminate noise, but samples with extremely low capacitance required 288 averages to reduce noise sufficiently. These measurements were done in parallel circuit mode rather than series circuit mode for two reasons: logically, our samples resemble a parallel circuit since capacitive and resistive features experience the AC signal at the same time rather than in sequence, and additionally because parallel mode permits the measurements of lower capacitance values than series mode does.

After the impedance measurements were collected, the perovskite samples were sent back to the University of Utah to have their thicknesses measured using profilometry. This is a process where a scrape is made across the surface of the sample, and a needle can trace the contours of the surface and scratch to gauge the depth. Fig. 4.1(a) displays a microscope image of a MAPI sample with a scratch across its surface for profilometry. The gold electrodes appear as white reflective lines across the image, and can be seen underneath the thin grains in the dark MAPI sample. Fig. 4.1(b) shows the 5 profilometer needle paths that were selected to compare the depths of the MAPI surface,

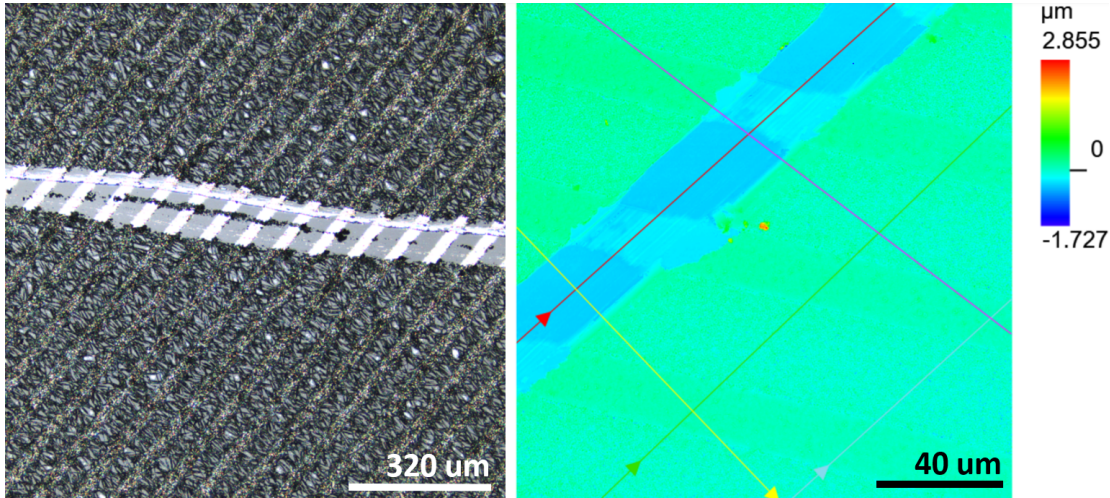


Figure 4.1 (a) Microscope image of MAPI perovskite grown on interdigitated electrode substrate with a large scratch in the middle for profilometry analysis. Electrode fingers appear as white stripes and can be seen underneath the dark MAPI structure. (b) Image from the profilometry software of the scratch in MAPI, where color represents approximate depth. Five trajectories given by colored arrows can be seen detailing the paths that the profilometer needle will take when gauging film thickness.

electrode surface, and quartz surface. Two samples of MAPI were found to have thicknesses of $390 (\pm 20)$ nm and $707 (\pm 56)$ nm.

4.2 Measurements on MAPI

Data on the MAPI perovskite samples can be seen in Fig. 4.2 below. The two published measurements by Anusca *et al.* [5] and Lin *et al.* [6] show similar general trends but have very different dielectric measurements overall, differing by more than a factor of two at high frequency. Our model predicts values that sit comfortably within this range which may be a good indication of accurate measurement.

Additionally, the two thicknesses of MAPI that were measured, shown in the second figure, are in reasonable agreement with each other. One predicts high frequency values of $\epsilon_r = 26.0$, and the other of $\epsilon_r = 31.7$. Both of these are quite similar to the values predicted by Lin *et al.* at this

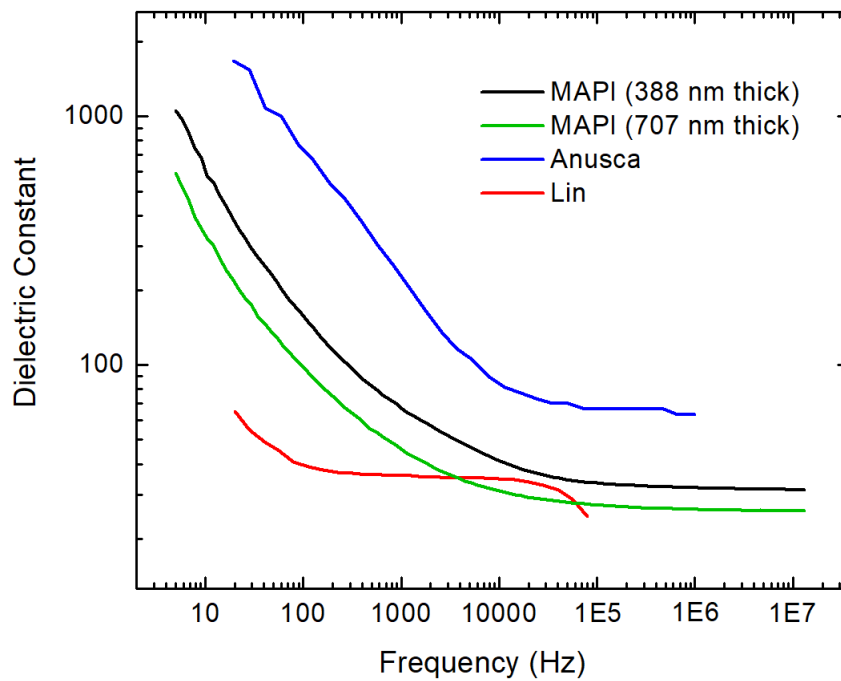


Figure 4.2 The values for calculated dielectric functions of MAPI thin film samples in black and green, compared to data taken from Anusca *et al.* [5] in blue and Lin *et al.* [6] in red.

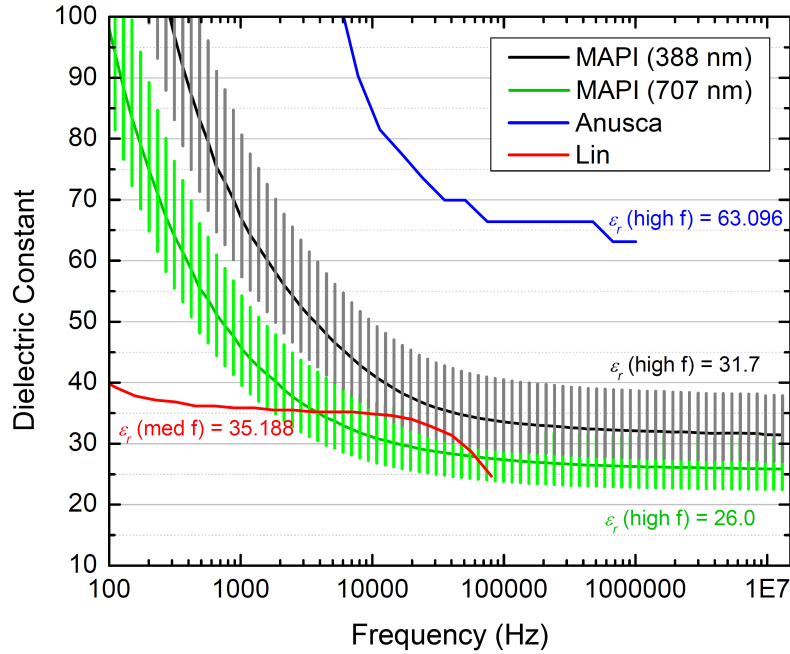


Figure 4.3 A closer look at values of calculated dielectric functions of MAPI thin film samples in black and green, compared to data taken from Anusca *et al.* [5] in blue and Lin *et al.* [6] in red. Error bars indicate uncertainty from layer thicknesses.

frequency range. A closer view of the high-frequency dielectric functions is shown in Fig. 4.3, with the addition of error bounds calculated from the uncertainty in thickness measurement.

4.3 Measurements on PEPI

The dielectric constant of PEPI perovskite thin films was measured on three different sample thicknesses: 568 nm, 716 nm, and 2527 nm. These measurements fall to a value of about $\epsilon_r = 7$ at high frequencies near 10 MHz, but show values in the hundreds and thousands at low frequencies; see Fig. 4.4.

A closer view of the high-frequency dielectric constant values with error bounds propagated from the uncertainty in thickness measurement are shown in Fig. 4.5. The thickest sample shows features that the other two do not, including a bump between 100 kHz and 1 MHz. This may

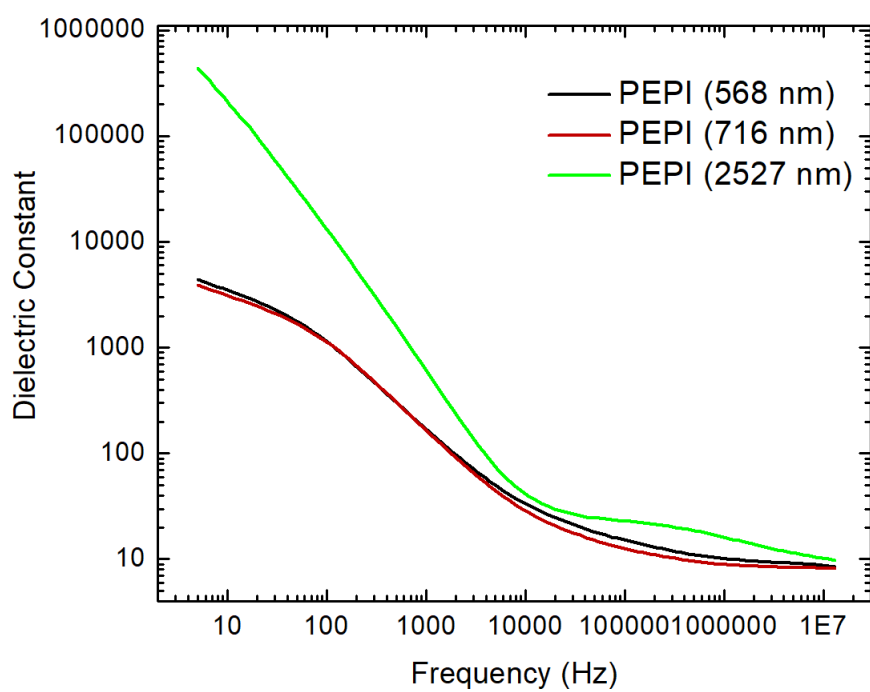


Figure 4.4 Calculated dielectric functions for PEPI perovskite thin films of three different thicknesses.

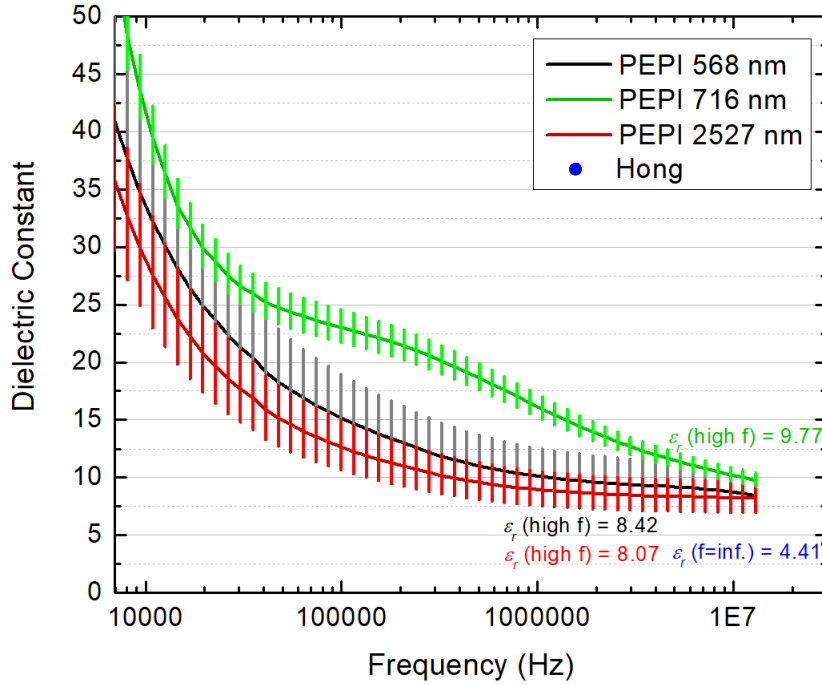


Figure 4.5 A closer view of our calculated dielectric functions for PEPI perovskite thin films of three different thicknesses. Vertical lines represent error bounds propagated from uncertainty in thickness measurement. The blue dot represents data taken from Hong *et al.* [8] for a frequency corresponding to 1.5 eV, which is below the electronic resonances but above the vibrational resonances (see Fig. 1.5).

be related to the formation of larger perovskite grains, since they are growing mostly above the electrodes rather than between them, so they have no size constraint.

4.4 Measurements on PEPBr and PEPCI

Dielectric function measurements were additionally performed on PEPBr and PEPCI perovskite thin films as shown in Fig. 4.6, though we are not aware of any published measurements of their dielectric constant in literature thus far. PEPBr was measured to have a dielectric constant of $\epsilon_r = 4.941$ near 10 MHz, and PEPCI around $\epsilon_r = 7.238$. Vertical lines represent error bounds propagated from uncertainty in thickness measurement. In the future, we will be able to provide

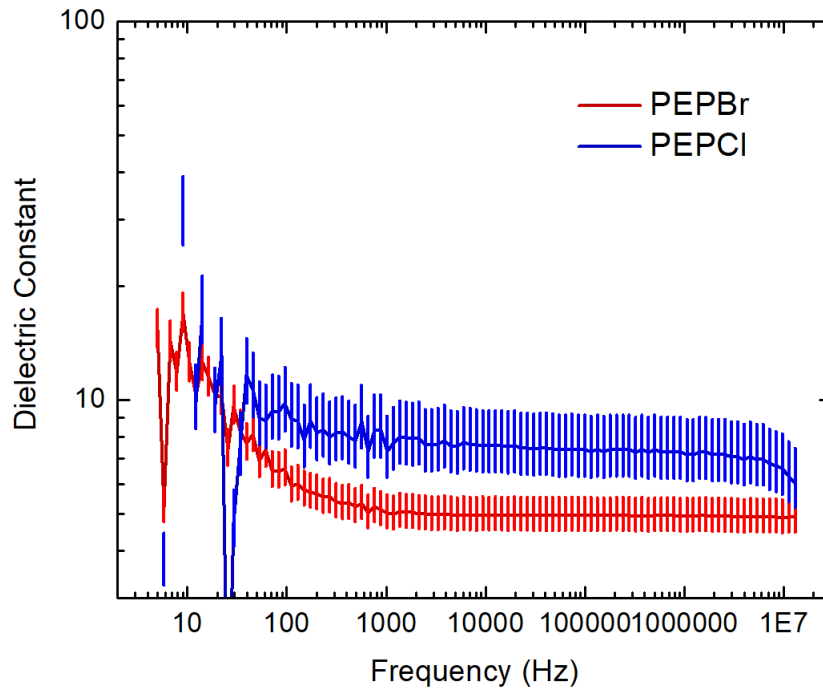


Figure 4.6 Calculated dielectric functions of PEPBr and PEPCl thin films. Lines represent error bounds propagated from uncertainty in thickness measurement.

some of the first low-frequency dielectric measurements on a wide variety of perovskite thin films due to the development of this model, as well as publish the model for others to use in different circumstances.

Chapter 5

Conclusion

5.1 Discussion

In this thesis, we developed a model capable of calculating the dielectric functions of thin film samples based on capacitance measurements from underlying electrodes. Due to the tightly-wound nature of IDEs, the electric field is confined near the surface of the electrodes, which allows greater sensitivity to thin film samples than is provided in most parallel-plate electrode geometries. Using this model, we were able to predict values for the dielectric constant on many materials such as quartz, water, and the perovskite thin films PEPI, MAPI, PEPBr, and PEPCl, and we compared these values against published values when available.

The results of this comparison indicate that this model provides a viable method to measure the dielectric functions of materials in proximity to IDEs due to good agreement with published values and consistency across many measurements. We report some of the first measurements of dielectric function on thin films PEPI, PEPBr, and PEPCl, and plan to report values for a wide variety of other samples in the future.

5.2 Future work

While this model is able to predict dielectric functions of various thin films already, there is more work that can be done to improve the measurements it makes, as well as provide more information about the samples it measures.

First, I would like to further analyze the results from this model by comparing its results to the results of other IDE models, such as that of Farnell *et al.* [19], while using the same capacitance data. This will allow us to gauge how successful our model is in comparison to existing IDE models.

In the coming months, we would like to obtain measurements on a series of varying n -number perovskite thin films, such as PEPI $n = 1, 2$, and 3. Analysis of measurements on a series like this would allow us to make important claims about the effect on lattice structure on dielectric constant, and consequently its effect on particles like excitons inside the crystal. It would also allow for a more accurate comparison of electroabsorption data on these film series, since the differences in dielectric constant between them could be accounted for.

Additionally, I have begun the work of extending these equations into three dimensions by using the dielectric tensor instead of assuming an isotropic dielectric constant. In theory, one should be able to solve these new equations for both the parallel and perpendicular dielectric constants of materials, as long as two different thicknesses of that material can be produced. This will allow us to make important insights about the anisotropy of the dielectric constant in perovskite materials, which will impact the comparison of electroabsorption in which the field is applied parallel to the perovskite layers to electroabsorption with field applied perpendicularly to the confining layers. (The latter involves the quantum confined Stark effect.)

There are many disciplines that the development of this IDE capacitance model may be able to benefit as more work is done, especially in the perovskite community, but also in materials science in general.

Bibliography

- [1] K. R. Hansen, C. E. McClure, J. S. Colton, and L. Whittaker-Brooks, “Franz-Keldysh and Stark Effects in Two-Dimensional Metal Halide Perovskites,” *PRX Energy* **1**, 013001 (2022).
- [2] K. R. Hansen *et al.*, “Low Exciton Binding Energies and Localized Exciton–Polaron States in 2D Tin Halide Perovskites,” *Advanced Optical Materials* p. 2102698 (2022).
- [3] “Best research-cell efficiency chart,” <https://www.nrel.gov/pv/cell-efficiency.html> (Accessed April 10, 2022).
- [4] J. N. Wilson, J. M. Frost, S. K. Wallace, and A. Walsh, “Dielectric and ferroic properties of metal halide perovskites,” *APL Materials* **7**, 010901 (2019).
- [5] I. Anusca *et al.*, “Dielectric Response: Answer to Many Questions in the Methylammonium Lead Halide Solar Cell Absorbers,” *Advanced Energy Materials* **7**, 1700600 (2017).
- [6] Q. Lin, A. Armin, R. C. R. Nagiri, P. L. Burn, and P. Meredith, “Electro-optics of perovskite solar cells,” *Nature Photonics* **9**, 106–112 (2015).
- [7] E. J. Juarez-Perez, R. S. Sanchez, L. Badia, G. Garcia-Belmonte, Y. S. Kang, I. Mora-Sero, and J. Bisquert, “Photoinduced Giant Dielectric Constant in Lead Halide Perovskite Solar Cells,” *The Journal of Physical Chemistry Letters* **5**, 2390–2394 (2014).

- [8] X. Hong, T. Ishihara, and A. U. Nurmikko, “Dielectric confinement effect on excitons in PbI_4 -based layered semiconductors,” *Physical Review B* **45**, 6961–6964 (1992).
- [9] M. Milanovic, G. Stojanovic, L. M. Nikolic, M. Radovanovic, B. Skoric, and A. Miletic, “Electrical and structural characterisation of nanostructured titania coatings deposited on interdigitated electrode system,” *Materials Chemistry and Physics* **130**, 769–774 (2011).
- [10] P. V. Torchyniuk, O. I. V’yunov, L. L. Kovalenko, A. A. Ishchenko, I. V. Kurdyukova, and A. G. Belous, “Influence of Solvent on Stability and Electrophysical Properties of Organic-Inorganic Perovskites Films $\text{CH}_3\text{NH}_3\text{PbI}_3$,” *Theoretical and Experimental Chemistry* **57**, 113–120 (2021).
- [11] L. Su, J. Mata-Contreras, P. Vélez, A. Fernández-Prieto, and F. Martín, “Analytical Method to Estimate the Complex Permittivity of Oil Samples,” *Sensors* **18**, 984 (2018).
- [12] A. Gennaro, O. Deschaume, H. Pfeiffer, C. Bartic, P. Wagner, and M. Wübbenhorst, “Understanding the Dehydration Stress in Lipid Vesicles by a Combined Quartz Crystal Microbalance and Dielectric Spectroscopy Study,” *Physica Status Solidi A* **217**, 1900986 (2020).
- [13] Z. Chen, A. Sepulveda, M. Ediger, and R. Richert, “Dielectric spectroscopy of thin films by dual-channel impedance measurements on differential interdigitated electrode arrays,” *European Physical Journal B* **85**, 268 (2012).
- [14] A. Risos, “Interdigitated Sensors: The Next Generation “Sensing Permittivity and Conductivity of Oils - Unaffected by Temperature”,” *IEEE Sensors Journal* **18**, 3661–3668 (2018).
- [15] R. C. Hensel, M. A. P. da Silva, A. Riul, and V. Rodrigues, “Dielectric Permittivity and Surface Charge Density in Layer-by-Layer Poly(diallyldimethylammonium chloride)/Poly(styrenesulfonate) Nanostructured Films: Implications for Biosensing,” *ACS Applied Nano Materials* **3**, 1749–1754 (2020).

- [16] T. M. Reader, U. Hanke, E. Halvorsen, and T. Grande, “A unified approach for the calculation of in-plane dielectric constant of films with interdigitated electrodes,” *Smart Materials and Structures* **29**, 115039 (2020).
- [17] Y. Zeng, R. Sanders, R. Wiegerink, and J. Lötters, “A Flow-Through Microfluidic Relative Permittivity Sensor,” *Micromachines* **11**, 325 (2020).
- [18] J. Oberländer, Z. B. Jildeh, P. Kirchner, L. Wendeler, A. Bromm, H. Iken, P. Wagner, M. Keusgen, and M. J. Schöning, “Study of Interdigitated Electrode Arrays Using Experiments and Finite Element Models for the Evaluation of Sterilization Processes,” *Sensors* **15**, 26115–26127 (2015).
- [19] G. W. Farnell, I. A. Cermak, P. Silvester, and S. K. Wong, “Capacitance and Field Distributions for Interdigital Surface-Wave Transducers,” *IEEE Trans. on Sonics and Ultrasonics* **SU-17**, 188–195 (1970).
- [20] H. N. Al-Shareef, D. Dimos, M. V. Raymond, R. W. Schwartz, and C. H. Mueller, “Tunability and Calculation of the Dielectric Constant of Capacitor Structures with Interdigital Electrodes,” *Journal of Electroceramics* **1**, 145–153 (1997).
- [21] H. Engan, “Excitation of Elastic Surface Waves by Spatial Harmonics of Interdigital Transducers,” *IEEE Transactions on Electron Devices* **ED-16**, 1014–1017 (1969).
- [22] M. W. den Otter, “Approximate expressions for the capacitance and electrostatic potential of interdigitated electrodes,” *Sensors and Actuators A* **96**, 140–144 (2002).
- [23] K. J. Binns, P. J. Lawrenson, and C. W. Trowbridge, *The Analytical and Numerical Solution of Electric and Magnetic Fields* (Wiley, New York, 1993), p. 532.

- [24] J. Krupka, K. Derzakowski, M. Tobar, J. Hartnett, and R. G. Geyer, “Complex permittivity of some ultralow loss dielectric crystals at cryogenic temperatures,” *Measurement Science Technology* **10**, 387–392 (1999).
- [25] A. De and K. V. Rao, “Dielectric properties of synthetic quartz crystals,” *Journal of Materials Science* **23**, 661–664 (1988).
- [26] F. Batalioto, A. R. Duarte, G. Barbero, and A. M. F. Neto, “Dielectric Dispersion of Water in the Frequency Range from 10 mHz to 30 MHz,” *Journal of Physical Chemistry* **114**, 3467–3471 (2010).
- [27] A. Angulo-Sherman and H. Mercado-Uribe, “Dielectric spectroscopy of water at low frequencies: The existence of an isopermittive point,” *Chemical Physics Letters* **503**, 327–330 (2011).